Modeling cross-shore sandbar behavior on the timescale of weeks

B. G. Ruessink,[1] Y. Kuriyama,[2] A. J. H. M. Reniers,[3,4] J. A. Roelvink,[4,5,6] and D. J. R. Walstra[4,6]

[1] We compare predictions of a coupled, wave-averaged, cross-shore waves-currents-bathymetric evolution model to observations of onshore and offshore nearshore sandbar migration. The observations span a 10- and 44-day period with onshore/offshore bar migration at Duck, North Carolina, and at Hasaki, Kashima Coast, Japan, respectively, a 3.5-month period of onshore bar migration at Duck, and a 22-day period of offshore bar migration at Egmond, Netherlands. With best fit parameter values the modeled temporal evolution of the cross-shore bed profiles agrees well with the observations. Model skill, defined as 1 minus the ratio of prediction to no-change error variances, ranges from 0.50 at Egmond to 0.88 for the prolonged onshore bar migration at Duck. Localized (in time and space) reductions in model skill coincide with alongshore variations in the observed morphology. Consistent with earlier observations, simulated offshore bar migration takes place during storms when large waves break on the bar and is due to the feedback between waves, undertow, suspended sediment transport, and the sandbar. Simulated onshore bar migration is predicted for energetic, weakly to nonbreaking conditions and is due to the feedback between near-bed wave skewness, bedload transport, and the sandbar, with negligible to small effects of bound infragravity waves and near-bed streaming. Under small waves and conditions, when breaking and nonbreaking conditions alternate with the tide, the sandbar is predicted to remain stationary. The intersite differences in the optimum parameter values are, at least partly, induced by insensitivity to parameter variations, parameter interdependence, and errors in the offshore wave forcing.

1. Introduction

[2] Waves, currents, and sediment transport in the nearshore depend strongly on bathymetry. When sediment flux gradients modify this bathymetry (e.g., on/offshore sandbar migration), subsequent wave and current patterns are altered as well. This, in turn, may lead to further modifications of the batyhmetry. The coupled waves-currents-bathymetry behavior has been observed in laboratory [e.g., *Stive and Battjes*, 1984; *Dally*, 1987; *Roelvink and Stive*, 1989] and

field [*Thornton et al.*, 1996; *Gallagher et al.*, 1998; *Hoefel and Elgar*, 2003] experiments. Nonetheless, coupled process models struggle to reproduce natural bar behavior on timescales of a few days to weeks [*Van Rijn et al.*, 2003; *Plant et al.*, 2004] and have uncertain skill on longer scales [*Roelvink et al.*, 1995; *Van Rijn et al.*, 2003]. Most of these models predict the amount of beach erosion under breaking waves but cannot address the subsequent recovery of a beach profile (e.g., onshore bar migration) under relatively quiescent wave conditions because of missing relevant processes [*Roelvink and Brøker*, 1993; *Van Rijn et al.*, 2003]. The development and objective testing of a more realistic waves-currents-bathymetric evolution model thus remains a challenging research goal.

[3] During the last decade considerable progress has been made in the identification of hydrodynamic processes relevant to on/offshore bar migration using noncoupled process models. In such models, times series of near-bed hydrodynamics measured at several locations over a bar are input into a sediment transport model; bathymetric change is then computed from continuity. The bed level evolution does not feed back to the hydrodynamics; instead, time series measured at the next time step are used. In this way, *Gallagher*

---

[1]Institute for Marine and Atmospheric Research Utrecht, Department of Physical Geography, Faculty of Geosciences, Utrecht University, Utrecht, Netherlands.

[2]Littoral Drift Division, Marine Environment and Engineering Department, Port and Airport Research Institute, Yokosuka, Japan.

[3]Division of Applied Marine Physics, Rosenstiel School of Marine and Atmospheric Science, University of Miami, Miami, Florida, USA.

[4]Faculty of Civil Engineering and Geosciences, Delft University of Technology, Delft, Netherlands.

[5]UNESCO-IHE Institute for Water Education, Delft, Netherlands.

[6]Marine and Coastal Management, WL/Delft Hydraulics, Delft, Netherlands.

et al. [1998] showed how the feedback between the breaking-induced undertow and the sandbar (at Duck, N. C.) caused the sandbar to move offshore during a storm. The undertow and associated current-related suspended sediment transport had a local maximum at or just shoreward of the bar, which, through conservation of sediment, forced the bar to move offshore. Consequently, the undertow and transport maximum shifted offshore as well, causing a continued offshore bar migration until the waves became too low to break on the bar. On the basis of the same Duck data, *Hoefel and Elgar* [2003] suggested that the asymmetry of forward pitched, breaking waves is responsible for onshore bar migration under mild wave conditions. Using a different sediment transport model but still the same data set, *Henderson et al.* [2004] found boundary layer streaming and Stokes drift to be essential to the prediction of onshore bar migration as well. Recently, *Plant et al.* [2006] hypothesized that horizontal flow patterns associated with alongshore nonuniformities in the sandbar commonly present under mild wave conditions [e.g., *Ranasinghe et al.*, 2004] are important to facilitate onshore sediment transport and bar migration. In their opinion, the alongshore uniform view on onshore bar migration rather than missing cross-shore sediment transport processes is the primary reason why coupled and noncoupled cross-shore models struggle to produce realistic predictions after storms.

[4] The development of coupled models, in which bathymetric change does feedback to affect the hydrodynamics at the next time step, dates back to the 1980s and early 1990s. Many of the earlier models used empirical expressions for sediment transport, disregarding the underlying flow systems. *Dally and Dean* [1984] and *Stive and Battjes* [1984] were among the first to implement a description of the breaking-induced undertow for modeling erosional events. *Stive* [1986] extended his earlier model to include onshore transport due to the skewness (relatively sharp crests and broad flat troughs) of nonbreaking waves, *Roelvink and Stive* [1989] and *Sato and Mitsunobu* [1991] examined the contribution of wave grouping-induced long-wave flow to the total sediment transport, and *Trowbridge and Young* [1989] and *Brøker Hedegaard et al.* [1991] suggested that boundary layer streaming is important to onshore transport, in particular during nonbreaking conditions. Surprisingly, detailed comparisons of modeled and natural bed evolution are scarce. In addition, most studies focused on the relevance of a single flow mechanism for cross-shore profile evolution [e.g., *Trowbridge and Young*, 1989], or examined either onshore [e.g, *Long et al.*, 2004] or offshore [e.g., *Van Rijn et al.*, 2003] bar migration. *Plant et al.* [2004] could hindcast individual onshore and offshore bar migration events observed at Duck reasonably accurately, but found their model to have little skill (relative to a no-change model) in reproducing a combined on/offshore event.

[5] In this paper, we develop and test a coupled, wave-averaged, cross-shore process model to hindcast observed natural sandbar behavior on the timescale of weeks, including storms and their intermediate low-energy conditions. Included hydrodynamical processes affecting sandbar migration are near-bed wave skewness, bound infragravity waves, undertow, and boundary layer streaming. We test model skill for data sets acquired at the barred beaches of Duck (N. C., USA), Hasaki (Kashima Coast, Japan), and Egmond (Netherlands). For each data set the best fit values of the free model parameters are obtained by minimizing the squared difference between observed and predicted bed evolution using an objective, global search algorithm.

2. Model Description

[6] The model comprises coupled, wave-averaged equations of hydrodynamics (waves and mean currents), sediment transport, and bed level evolution. Straight, parallel depth contours are assumed throughout. Starting with an initial, measured cross-shore depth profile and boundary conditions offshore, the cross-shore distribution of the hydrodynamics and sediment transport are computed. Transport divergence yields bathymetric changes, which feed back to the hydrodynamic model at the subsequent time step, forming a coupled model for bed level evolution. In the following, a summary of the main wave, flow, and sediment transport equations is presented. All variables are, unless stated otherwise, a function of the cross-shore location (x) and the slowly varying timescale of the morphology $(\bar{t})$.

2.1. Waves

[7] With the assumption that the wavefield spectrum is narrow in frequency and direction, the balance for the short-wave energy E_w is

$$\frac{\partial}{\partial x}\left(E_w c_g \cos\theta\right) = -D_b - D_f, \tag{1}$$

where c_g is the group velocity, θ is the wave angle from shore normal, and D_b and D_f are breaking-wave dissipation and bottom friction, respectively. The breaking-wave dissipation is modeled according to *Battjes and Janssen* [1978], as modified by *Roelvink et al.* [1995]. The dissipation parameter α, included in the parameterization of D_b, was set to 1, while for the wave height-to-depth parameter γ the parameterization by *Ruessink et al.* [2003] was adopted. This parameterization was preferred over the more traditional *Battjes and Stive* [1985] formulation, which overpredicts the wave height in sandbar troughs. Bottom friction is not important for surf zone wave energy dissipation (i.e., equation (1), $D_f \ll D_b$). Linear wave theory is used to compute c_g and Snell's law is used to determine $\theta(x)$ from offshore measurements.

[8] The breaking-wave dissipation feeds into the balance for roller energy E_r [*Nairn et al.*, 1990; *Stive and De Vriend*, 1994],

$$\frac{\partial}{\partial x}(2E_r c \cos\theta) = -D_r + D_b, \tag{2}$$

where c is the phase speed. The roller dissipation D_r is given by

$$D_r = \frac{2gE_r \sin\beta}{c}, \tag{3}$$

where g is gravitational acceleration and $\beta = 0.1$ [*Nairn et al.*, 1990; *Reniers and Battjes*, 1997] is the roller slope.

[9] The wave setup η is determined from the depth-integrated and time-averaged cross-shore momentum balance equation,

$$\rho g h \frac{\partial \eta}{\partial x} + \frac{\partial S_{xx}}{\partial x} = 0, \tag{4}$$

where ρ is water density, h is the total water depth, and the wave radiation stress $S_{xx} = (n + n\cos^2\theta - 0.5)E_w + 2E_r\cos^2\theta$, with $n = c_g/c$. In equation (4), the effect of the mean shear stress at the bed due to currents and of cross-shore winds on the cross-shore set-up pattern is ignored.

2.2. Currents

[10] The vertical distribution of the alongshore and cross-shore mean current is determined by solving the horizontal momentum balance. Here, *Reniers et al.*'s [2004] flow model is used, a quasi-3D model that identifies a surface layer above the wave trough level, a middle layer between the wave trough level and the top of the wave boundary layer, and the wave boundary layer itself. Alongshore currents are driven by the off-diagonal component of the incident wave-radiation stress tensor S_{xy} including the roller contribution, and are logarithmic under non-breaking conditions and become more depth-uniform under breaking conditions. Because of the importance of the cross-shore mean current to on/offshore bar migration, a more detailed description of the cross-shore current modeling is presented in the following. For additional details, we refer to *Reniers et al.* [2004].

[11] The curvature (in the vertical) of the cross-shore flow results from the vertical imbalance between the cross-shore wave radiation stress gradient and the pressure gradient owing to wave set-up. This drives a circulation current with a shoreward wave-induced mass flux above the wave trough level and a seaward return flow (undertow) below this level, with the depth-integrated return flow ($\overline{u}$) equal to the wave-induced mass-flux,

$$\overline{u} = -\frac{E_w + 2E_r}{\rho c h_t} \cos\theta, \tag{5}$$

where h_t is the water depth below the wave trough. The velocity gradients in the middle and bottom layer are related to the shear stress τ_x through the turbulent eddy viscosity v_t,

$$\tau_x = \frac{\rho v_t}{h} \frac{\partial u}{\partial \sigma}, \tag{6}$$

where σ is nondimensional depth increasing from 0 at the bed to 1 at the top of the middle layer. The shear stress τ_x in the middle layer is

$$\tau_x = \tau_s - R_x(1 - \sigma), \tag{7}$$

where $\tau_s = D_r\cos\theta/c$ is the breaking-wave stress at the top of the middle layer and R_x is the depth-invariant forcing by the pressure gradient owing to wave-setup.

[12] Near the bed, boundary layer effects become important. The nonuniformity of the boundary layer under a wave, which is proportional to D_f [*Trowbridge and Young*,

1989; *Fredsøe and Deigaard*, 1992], results in an additional time-averaged shear stress component,

$$\tau_x = \tau_s - R_x(1 - \sigma) + \frac{D_f \cos\theta}{c} \frac{(\delta - h_t\sigma)}{\delta}, \tag{8}$$

where δ is the thickness of the wave bottom boundary layer [*Bosboom et al.*, 1997]. In the absence of breaking waves the third term on the right-hand-side of equation (8) results in an onshore directed current in the bottom boundary layer, known as streaming. Once wave breaking becomes important, the resulting set-up gradient within the surf zone dominates the force balance in the bottom boundary layer, resulting in an offshore directed flow close to the bed.

[13] The vertical distribution of the eddy viscosity ν_t in equation (6) is implemented as the product of a parabolic shape function and a scale factor, which are different for the middle and bottom layer. In the former, the scale factor is the depth-averaged viscosity $\overline{\nu}_t$,

$$\overline{\nu}_t = \alpha_w H_{rms} \left(\frac{D_r}{\rho}\right)^{1/3}, \tag{9}$$

where α_w is a free model parameter. The eddy viscosity is 0 at the bed and maximum at the sea surface. In the bottom boundary layer, the viscosity produced by equation (9) is locally enhanced by another parabolically shaped viscosity profile (see *Reniers et al.* [2004] for further details). The flow model is solved on 20 log-spaced grid points, spanning the water column from a height Z above the bed of 1 cm to $Z = h$.

2.3. Sediment Transport and Bottom Changes

[14] The net sediment flux q_{net} is the sum of the bedload transport flux q_{bed} and the current-related suspended load transport flux $q_{s,c}$,

$$q_{net} = q_{bed} + q_{s,c}. \tag{10}$$

[15] The bedload transport flux is implemented on the basis of *Ribberink* [1998] and *Van Rijn* [1995] and is expressed as

$$q_{bed}(\overline{t}) = \langle q_{bed}(t)\rangle, \tag{11}$$

where

$$q_{bed}(t) = 9.1\beta_s \left[|\theta'(t)| - \theta_{c,s}\right]^{1.8} \frac{\theta'(t)}{|\theta'(t)|} \sqrt{\Delta g d_{50}^3} \tag{12}$$

with $q_{bed}(t) = 0$ if $|\theta'(t)| \leq \theta_{c,s}$. The calculation of $q_{bed}(\overline{t})$ thus requires the time-average ($\langle\rangle$) of an instantaneous (intrawave) time series of the dimensionless effective shear stress $\theta'(t)$ due to currents and waves, which is parameterized here as

$$\theta'(t) = \frac{0.5\rho f'_{cw}|u_b(t)|u_b(t)}{(\rho_s - \rho)g d_{50}}, \tag{13}$$

where ρ_s is the sediment density, f'_{cw} is a friction factor [*Van Rijn*, 1993], d_{50} is the median grain size, and $u_b(t)$ is a time

series of the near-bed intrawave near-bottom horizontal velocity of the combined wave-current motion. This series is constructed to have the same characteristics of short-wave velocity skewness, amplitude modulation, bound infragravity waves, and mean flow as a natural random wavefield. To this end, $u_b(t)$ is made up of 3 components,

$$u_b(t) = u_{nl}(t) + u_{bw}(t) + \overline{u}_{lg}. \tag{14}$$

The time series of nonlinear near-bed short-wave orbital motion u_{nl} is modeled according to the Fourier approximation of the stream function theory as developed by *Rienecker and Fenton* [1981]. As input the local root-mean square wave height, peak period, and water depth are used. The resulting series has nonzero skewness but zero acceleration skewness (asymmetry). The computation of the bound-infragravity series $u_{bw}(t)$ is based on the method of *Sand* [1982] (see *Roelvink and Stive*, [1989] for details). The magnitude of the offshore directed bound-infragravity transport can be scaled with the parameter c_r, which changes the phase between the wave group and the infragravity motion from $-180°$ (maximum offshore transport, $c_r = 1$) to $-90°$ (no transport, $c_r = 0$). The mean-flow component in equation (14), $\overline{u}_{lg}$, is the time-averaged horizontal velocity at the lowest computational grid point in the flow model. With this term, the contribution of the mean flow in the wave boundary layer to the bedload is considered. As indicated in Section 2.2, its cross-shore component ($\overline{u}_{lgx}$) is typically onshore directed under nonbreaking waves owing to streaming and offshore directed in surfzone conditions.

[16] Returning to equation (12), $\Delta = (\rho_s - \rho)/\rho$, and β_s is the Bagnold parameter

$$\beta_s = \frac{\tan \phi}{\tan \phi + \frac{u_{bx}(t)}{|u_b(t)|} \frac{\partial z}{\partial x}}. \tag{15}$$

The parameter $\tan\phi$ is the tangent of the angle of repose and $u_{bx}(t)$ is the cross-shore component of $u_b(t)$. Finally, $\theta_{c,s}$ is the slope-corrected value of the nondimensional critical shear stress θ_c, for which the parameterization by *Van Rijn* [1993] is adopted. The slope-correction is made using the Schoklitsch factor [e.g., *Van Rijn*, 1993],

$$\theta_{c,s} = \frac{\sin\left[\phi + \arctan\left\{\frac{u_{bx}(t)}{|u_b(t)|} \frac{\partial z}{\partial x}\right\}\right]}{\sin \phi} \theta_c. \tag{16}$$

[17] The current-related suspended sediment transport rate is given by

$$q_{s,c} = \frac{\int_{Z_a}^{h} c(Z)u(Z)\,\partial Z}{\rho_s}, \tag{17}$$

where Z_a is a near-bed reference height, and $c(Z)$ and $u(Z)$ are the vertical profiles of the time-averaged concentration and cross-shore mean-current, respectively. The former profile, $c(Z)$, is computed from the time-averaged convection-diffusion equation, which is solved by numerical integration from Z_a to the water surface (see *Van Rijn* [1993] for further details). At Z_a, a reference

concentration c_a is specified as boundary condition [*Van Rijn*, 1993]

$$c_a = 0.015\rho_s \frac{d_{50}}{Z_a} \frac{T^{1.5}}{D_*^{0.3}}, \tag{18}$$

in which $D_* = d_{50} \left[(\rho_s/\rho - 1)g/\nu^2\right]$ (ν is the kinematic viscosity $\approx 10^{-6}$ m²/s) and T is a nondimensional bed-shear stress parameter [*Van Rijn*, 1993]. The computation of T requires the specification of the wave-related roughness k_w, for which we take $2.5d_{50}$ [*Soulsby*, 1997]. Following *Van Rijn* [1993], Z_a is set equal to the current-related roughness k_c.

[18] Finally the bottom changes are obtained from continuity,

$$\frac{\partial z(x,\overline{t})}{\partial \overline{t}} = -\frac{1}{1-p} \frac{\partial q_{net}(x,\overline{t})}{\partial x}, \tag{19}$$

where $p = 0.4$ is the assumed bed porosity. The most landward wet computational grid point at each time step is taken as the grid point where the nondimensional wave period $T_p\sqrt{g/h}$ exceeds 40 for the first time. For $T_p = 7$ s, for example, this implies that no hydrodynamical and transport computations are carried out in depths less than about 0.30 m. The sediment transport rate at the last wet grid point is translated into an offshore (negative q) or onshore (positive q) advection of the dry grid points; the shape of the dry beach remains unaltered. Equation (19) is solved on a 4-point Preismann implicit scheme.

2.4. Parameter Optimization

[19] The fate of a model simulation is to a large extent determined by the value of the free parameters. The parameters in the wave model have been estimated before for a wide range of conditions [e.g., *Ruessink et al.*, 2003], leading to the conclusion that they can be set to values existing in the literature. Thus the model is employed by allowing adjustments in model output by the parameters in the flow model (α_w) and the sediment transport equations ($\tan\phi$, c_r, k_c) only. The roughness k_w is not implemented as a free parameter; *Ruessink* [2005] showed how the inclusion of both k_w and k_c in a model fitting procedure resulted in an ill-posed optimization problem because of strong $k_w - k_c$ interaction through equation (18) (k_w affects c_a through the nondimensional bed shear stress T, and k_c through the reference height Z_a). The friction factor f'_{cw} is computed [*Van Rijn*, 1993] using values of k_w and k_c, and, accordingly, is not a free model parameter itself.

[20] All four free parameters affect the magnitude (and sign) of $q_{net}(x, \overline{t})$, α_w and k_c through $q_{s,c}(x, \overline{t})$, and $\tan\phi$ and c_r through $q_{bed}(x, \overline{t})$. With an increase in α_w, the vertical cross-shore velocity profiles vary more slowly with depth, implying lower (offshore-directed) mean flows near the bed (where sediment concentrations are largest). Thus, with an increase in α_w, $q_{s,c}$ reduces. The primary effect of k_c is to change the reference height in the computation of $q_{s,c}$. With an increase in k_c, this height increases, reducing the reference concentration c_a and, consequently, $q_{s,c}$. A decrease in $\tan\phi$ hinders upslope transport and stimulates downslope transport, leading to a slightly less pronounced bar-trough relief. Finally, an increase in c_r increases the offshore bedload transport by bound infragravity waves.
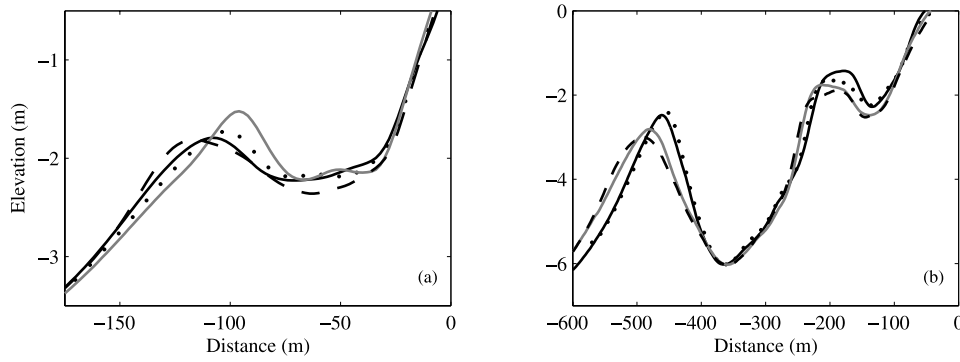
Figure 1. Measured elevation versus cross-shore distance at (a) Duck on 24 September (solid line), 26 September (dotted line), 30 September (shaded line), and 4 October 1994 (dashed line) and (b) Egmond on 16 October (solid line), 19 October (dotted line), 4 November (shaded line), and 7 November 1998 (dashed line).

[21] In the present work, the global search Shuffled Complex Evolution (SCE-UA) algorithm [*Duan et al.*, 1993] was applied to find optimum parameter values ($\mathbf{p}_{opt}$) for a given data set. To find the optimum parameter set, SCE-UA minimizes the least squares function F,

$$F(\mathbf{p}) = \sum_{x,\bar{t}} \left(z_{model}(x,\bar{t}|\mathbf{p}) - z_{obs}(x,\bar{t}) \right)^2, \qquad (20)$$

where the subscripts "model" and "obs" represent model-predicted and observed values, respectively. Convergence to $\mathbf{p}_{opt}$ was declared here once SCE-UA was unable to reduce $F(\mathbf{p})$ by more than 0.1% during a user-specified number of simulations or once the number of simulations exceeded 1500.

[22] With $\mathbf{p}_{opt}$, model skill R is estimated as

$$R(\bar{t}) = 1 - \frac{\epsilon_{model}^2(\bar{t})}{\epsilon_{persistence}^2(\bar{t})}, \qquad (21)$$

with

$$\epsilon_{model}^2(\bar{t}) = \sum_{x,\bar{t}} \left(z_{model}(x,\bar{t}|\mathbf{p}_{opt}) - z_{obs}(x,\bar{t}) \right)^2 \qquad (22)$$

and

$$\epsilon_{persistence}^2(\bar{t}) = \sum_{x,\bar{t}} \left(z_{obs}(x,\bar{t}) - z_{obs}(x,\bar{t}=\bar{t}_0) \right)^2. \qquad (23)$$

The model skill equals 1 when the model predictions and the observations are in perfect agreement and reduces to 0 when the model error ϵ_{model}^2 is equal to the persistence error $\epsilon_{persistence}^2$. In case the model performs worse than the no-change model, R becomes negative.

3. Observations and Model Setup

3.1. Observations

[23] Bathymetric data used in this paper to evaluate the model were collected during four experiments at the single-barred beaches at Duck, N. C., USA (Duck94 and Duck 1982 experiments) and at Hasaki, Kashima Coast, Japan, and at the double-barred beach at Egmond, Netherlands. The selected Duck94 and Hasaki data set comprise combined on/offshore bar migration events during a 10- and 44-day period, respectively. In the Duck94 experiment the sandbar moved onshore by about 12 m during swell waves, while during the subsequent more energetic seas the bar migrated some 20 m in the seaward direction (Figure 1a). The Hasaki data set is characterized by a sandbar that migrated about 75 m offshore during 3 high-wave events (up to 20 m/day) and moved onshore at rates of 0 to 6 m/day during the intermediate, less energetic conditions (Figure 2a). Note that the cross-shore distance between the −4 m elevation contour shoreward and seaward of the bar crest at Hasaki varied with time. This indicates bar steepening during the storms (reduction in distance) and bar flattening during the intermediate low-energy conditions (increase in distance). In the Duck 1982 data the sandbar migrated 65 m in the onshore direction during a 3.5-month period (Figure 3a), while both sandbars in the Egmond migrated some 30 m offshore (Figure 1b) during a 22-day series of high-wave events. In most cases, onshore bar migration resulted in a bar-trough relief reduction (see, e.g., Figure 3a, with a 50% reduction in bar-trough height during the Duck 1982 experiment), while the bar often became more pronounced when it moved offshore, generally because of a deepening of the trough (e.g., Figure 2a around $\bar{t} = 50$ and 70 days). Extensive site and data set descriptions are given by *Gallagher et al.* [1998] for Duck94, *Trowbridge and Young* [1989] for Duck 1982, *Kuriyama* [2002] for Hasaki, and *Ruessink et al.* [2000] for Egmond.

[24] In all data sets the cross-shore mean change between consecutive surveys, computed as (see, e.g., Figures 2b and 3b)

$$\Delta_{net} = \frac{1}{N_x} \sum_{i=1}^{N_x} \Delta_i, \qquad (24)$$

where Δ_i is the measured change in bed level at cross-shore position i, was at least a factor 2−4 less than the root-mean square changes,

$$\Delta_{rms} = \sqrt{\frac{1}{N_x} \sum_{i=1}^{N_x} \Delta_i^2}, \qquad (25)$$

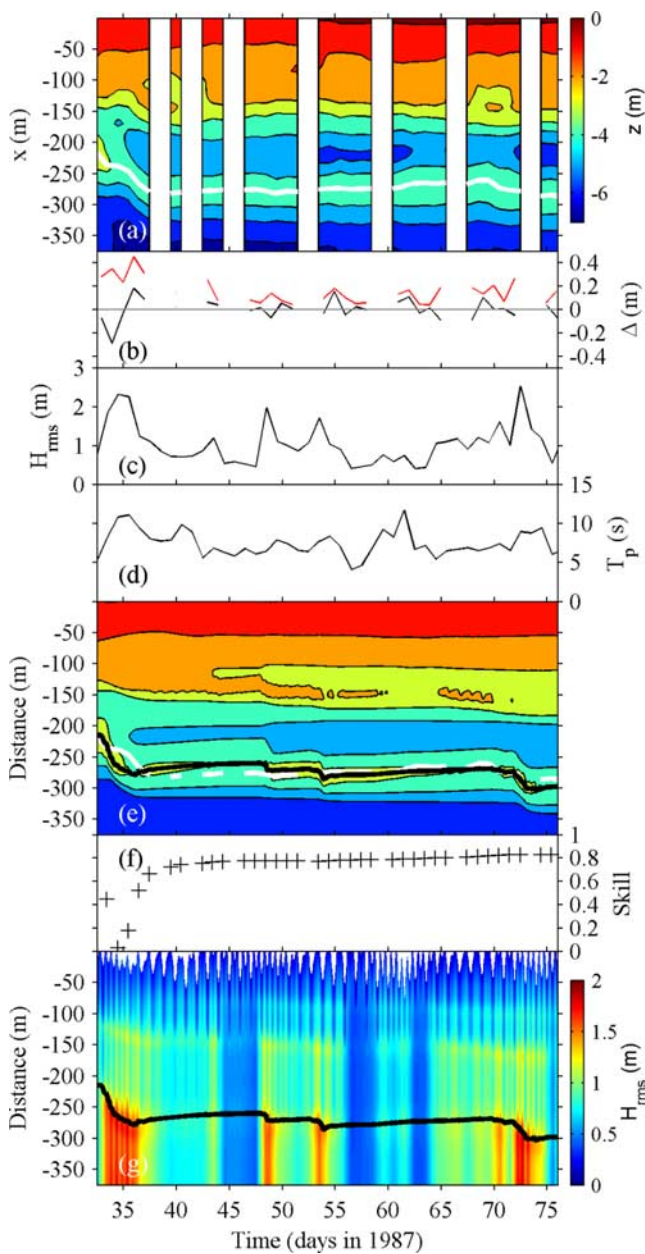**Figure 2.** Measured (a) seafloor elevation, (b) net (black line) and rms (red line) elevation change (Δ_{net} and Δ_{rms}, respectively), (c) offshore root mean square wave height H_{rms}, and (d) offshore peak period T_p versus time at Hasaki. Model results are provided in Figures 2e–2g: (e) predicted seafloor elevation, (f) model skill R, and (g) root mean square wave height H_{rms} versus time. All model results are based on the optimum parameter set. The white lines in Figure 2a and 2e are the measured sandbar crest location. The predicted location is indicated by the black lines in Figures 2e and 2g.

study area (Figure 4). These images also show the persistent presence of beach megacusps with alongshore length scales of $O(100)$ m with superimposed $O(10)$ m beach cusps, and the attaching of the bar to the beach north of the study area. Whether these nonuniformities in morphology affected sandbar evolution and flow patterns in the survey area is
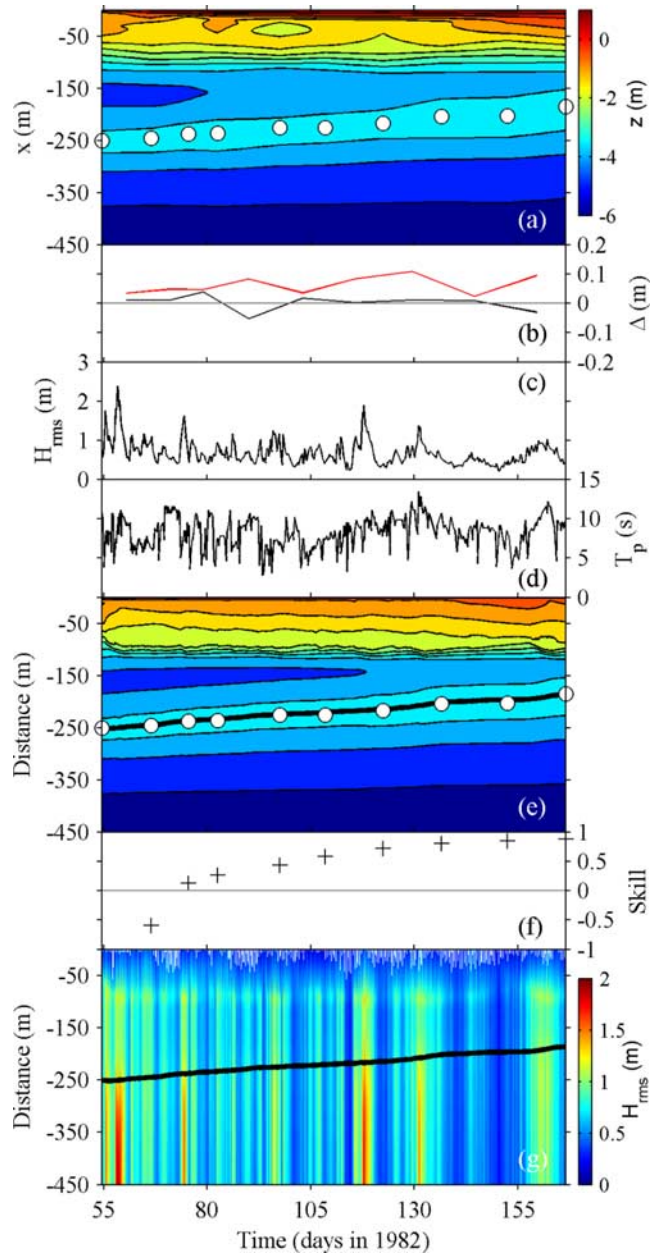

Figure 3. Measured (a) seafloor elevation, (b) net (black line) and rms (red line) elevation change (Δ_{net} and Δ_{rms}, respectively), (c) offshore root mean square wave height H_{rms}, and (d) offshore peak period T_p versus time at Duck. Model results are provided in Figures 3e–3g: (e) predicted seafloor elevation, (f) model skill R, and (g) root mean square wave height H_{rms} versus time. All model results are based on the optimum parameter set. The white dots in Figures 3a and 3e are the measured sandbar crest locations. The predicted location is indicated by the black lines in Figures 3e and 3g.

If sand is conserved in the profile, $\Delta_{net} = 0$. The dominance of Δ_{rms} over Δ_{net} implies that sediment was predominantly redistributed in the cross-shore direction. For the Duck94 data, this is in line with analyses of altimeter-derived depth evolution in a single cross-shore line [*Gallagher et al.*, 1998] and is confirmed from visual inspection of available 10-minute time exposure video images overlooking the

Figure 4. Time exposure video images showing Duck94 morphology on (a) 26 September 2100 UT ($\bar{t} \approx$ 268.5 days), (b) 30 September 1500 UT ($\bar{t} \approx$ 272.5 days), and (c) 4 October 1800 UT ($\bar{t} \approx$ 276.5 days). The arrows indicate the approximate alongshore location of the main cross-shore instrument array [*Gallagher et al.*, 1998]. The seaward white band, resulting from preferred wave breaking, indicates the approximate position of the sandbar. *Ruessink et al.*'s [2001] findings of alongshore uniformity in the sandbar [*Ruessink et al.*, 2001, Figure 9] were based on bathymetric surveys collected in a 350 m wide alongshore region centered around the main array, excluding the steep beach face.

not known. The inner Egmond bar possessed a crescentic planshape throughout the experiment with an alongshore length scale of about 600 m and a cross-shore amplitude less than 20 m, while the outer Egmond bar was alongshore uniform [*Ruessink et al.*, 2000]. Despite the inner-bar alongshore variability, modeled (based on the assumption of alongshore uniform morphology) and measured alongshore currents across the inner bar compared well [*Ruessink et al.*, 2001] for the time period selected here. This suggests that alongshore nonuniform effects on alongshore currents (such as local alongshore pressure gradients) and, presumably, on sandbar variability as well are small relative to cross-shore effects. Although sediment was conserved for the entire Hasaki data set ($\Delta_{net} \approx 0$ m), there were a few periods when alongshore processes may have dominated over cross-shore processes and/or when the sediment flux past the offshore boundary was nonzero. For instance, the $\Delta_{net} = -0.3$ m at $\bar{t} = 34$ days (Figure 2b) indicates a substantial loss of sediment during the first storm, which was, however, compensated by an almost identical gain 2 days later (Figure 2b). Time exposure X-band radar images collected hourly at Hasaki since 2002 [*Takewaka*, 2005] show that a bar located fairly close to the shore may contain crescentic structures that are erased during storms, while a bar located further offshore (like at the end of our data set) is generally alongshore uniform (S. Takewaka, personal communication, 2006). The latter is consistent with yearly, spatially extensive bathymetric surveys [*Kuriyama*, 2002]. Figures 2b, 3b, and 4, as well as existing bathymetric analyses of Duck 1982 [*Trowbridge and Young*, 1989] and Duck94 [*Ruessink et al.*, 2001] demonstrate that the Duck and Hasaki onshore bar migration events selected here were not associated with the development of alongshore variations and that, accordingly, the processes described by *Plant et al.* [2006] for onshore bar migration are not relevant in the present study.

[25] Time series of offshore wave height and period are provided in Figures 5a–5b for Duck94, Figures 2c–2d for Hasaki, Figures 3c–3d for Duck 1982, and Figures 6a–6b for Egmond. The time step between successive observations is 1 hour, except at Hasaki, for which daily averaged values were available only. Because the offshore wave sensor at Hasaki and during Duck 1982 was nondirectional, we had to assume a time-independent wave angle for these data

sets. We set the offshore wave direction to 30° from shore normal at Hasaki on the basis of wave climate considerations [*Kuriyama et al.*, 2005] and to 0° at Duck 1982 to be consistent with *Trowbridge and Young* [1989].

[26] At each site, hourly offshore water levels were available. The values for both Duck experiments were measured at the end of the pier at the Army Corps of Engineers' Field Research Facility (FRF), while the Egmond values were computed by averaging two tidal gauges located about 15 km north and south of Egmond. At Hasaki, the tidal station malfunctioned, so we used predicted water levels.
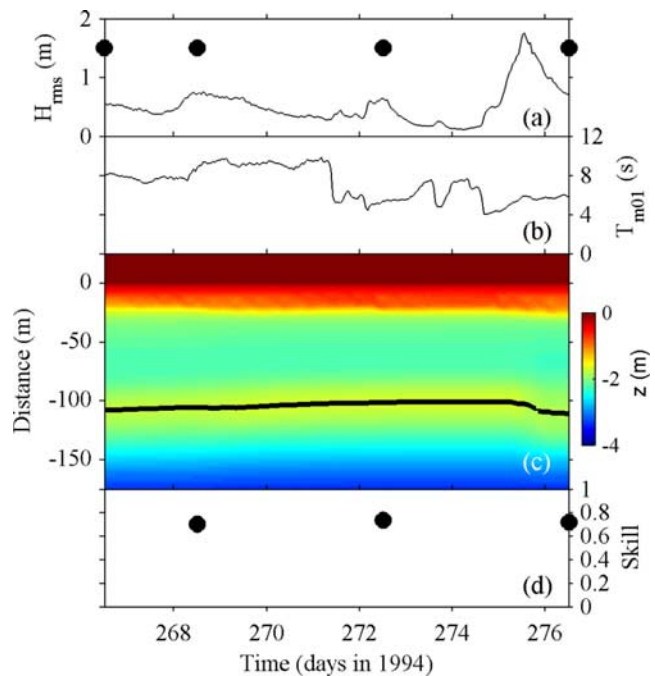

Figure 5. (a) Offshore root mean square wave height H_{rms}, (b) offshore centroidal period T_{m01}, (c) predicted seafloor elevation z, and (d) model skill R versus time at Duck. The model results are based on the optimum parameter set. The predicted sandbar crest location is indicated by the black line in Figure 5c. The dots in Figure 5a indicate the moments of spatially extensive bathymetric surveys.
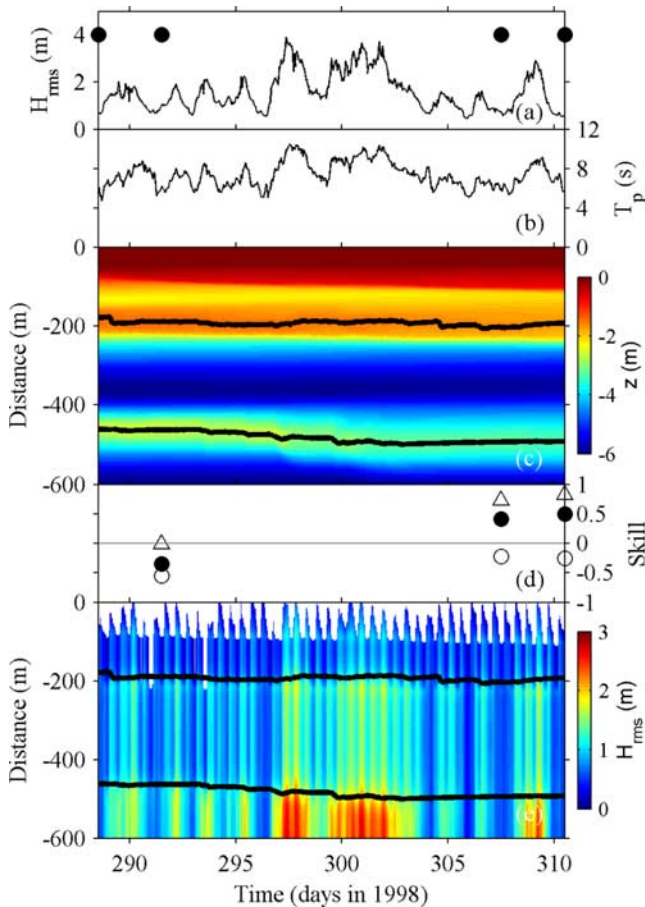
Figure 6. Measured offshore (a) root mean square wave height H_{rms} and (b) peak period T_p versus time at Egmond. Model results are provided in Figures 6c–6e: (c) predicted seafloor elevation, (d) model skill R (solid circles, entire x range; open circles, inner bar; and triangles, outer bar), and (e) root mean square wave height H_{rms} versus time. All model results are based on the optimum parameter set. The predicted sandbar crest location is indicated by the black lines in Figures 6c and 6e. The dots in Figure 6a indicate the moments of spatially extensive bathymetric surveys.

3.2. Model Setup

[27] In all simulations the cross-shore grid extended from the offshore wave sensor to the top of the foredune, well shoreward of the last wet grid point. The cross-shore grid size varied from several tens of meters in depths larger than $10–15$ m to 1 m on the intertidal beach. The d_{50} at Hasaki and Egmond is cross-shore constant at approximately 180 μm [*Katoh and Yanagishima*, 1995] and 265 μm [*Van Rijn et al.*, 2002], respectively. For the Duck94 experiment, the median grain size was, on the basis of *Stauble and Cialone* [1996], implemented as indicated in Figure 7. The rapid d_{50} increase around the low-water line is associated with the presence of a bi-modal gravel component along with sand size fractions. *Stauble and Cialone* [1996] further indicate that the fine sediments are removed from the foreshore in the seaward direction during storm conditions, leaving a coarse lag deposit in the trough and on the foreshore. Our model is not capable of handling sediment transport in a multifraction approach. To mimic the lag

deposit on the foreshore, the beach shoreward of $x = -18$ m (the approximate low-tide position, Figure 1) was implemented as a fixed layer where the bed level cannot erode below the level of the initial profile. Sedimentation on this layer, and subsequent erosion to the level of the initial profile is, however, permitted. Without the fixed layer, all Duck94 model simulations ended prematurely following unrealistic behavior of the steep foreshore. Although based on the Duck94 experiment, the z dependence of d_{50} as shown in Figure 7 was applied in the Duck 1982 simulations as well. In all simulations $\partial \bar{t}$ was set to 1 hour.

[28] The computation of equation (20) was based on the cross-shore range encompassing the active bar zone ($-204 \leq x \leq -48$ m for Duck94, $-375 \leq x \leq -30$ m for Hasaki, $-400 \leq x \leq -100$ m for Duck 1982, and $-600 \leq x \leq -30$ m for Egmond, with $x = 0$ m corresponding to the approximate location of $z = 0$ m in the initial profile and x defined positive onshore at all sites). We have excluded the offshore zone, where morphological change is minimal, and the intertidal zone because we have ignored processes in the swash zone (Section 2.3). Additionally, we have excluded the region between the inner trough and the intertidal beach at Duck to avoid any effect of the fixed layer on model skill.

4. Model Results

[29] With the best fit parameter settings estimated by the SCE-UA algorithm (Table 1) calculations of the temporal evolution of the cross-shore bed profiles agree well with the observations (Figure 8). The good agreement is reflected by the positive model skill at the end of all simulations, varying from 0.50 at Egmond (Figure 6d) to 0.88 for the Duck 1982 experiment (Figure 3f). The model is capable of reproducing the combined on/offshore events observed in the Duck94 and Hasaki data sets (Figures 5c and 2e, respectively), as well as of predicting the prolonged onshore and offshore outer-bar migration during Duck 1982 (Figure 3e) and at Egmond (Figure 6c), respectively. Also, the model
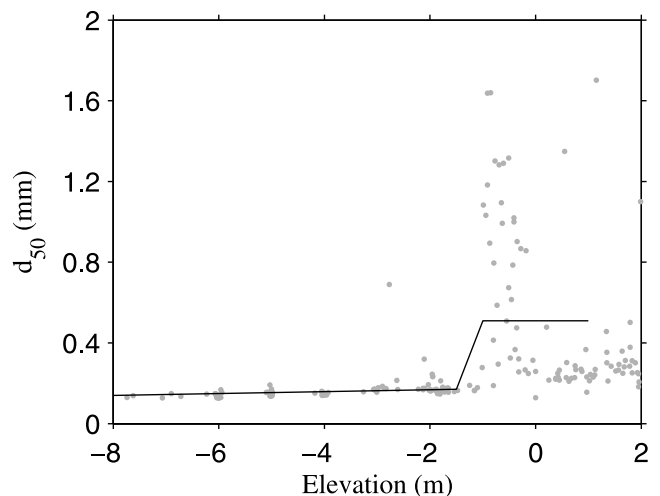

Figure 7. Median grain size d_{50} versus bed elevation z at Duck as sampled in August 1994 [*Stauble and Cialone*, 1996]. The solid line is the dependence of d_{50} on z as implemented in the Duck simulations.

Table 1. Optimized Parameter Estimates

Location	α_w	$\tan\phi$	c_r	k_c, m
Duck94	0.077	0.466	0.001	0.027
Hasaki	0.056	0.141	0.093	0.037
Duck 1982	0.120	0.253	0.011	0.059
Egmond	0.106	0.102	0.001	0.061

predicts accurately the trough deepening (Figure 2e, specifically at $\bar{t}$ = 50 and 70 days) and the temporal change in the steepness of the seaward bar flank at Hasaki (Figures 2e and 8d–8f), and the about 50% reduction in bar-trough relief during the Duck 1982 experiment (Figures 8g–8i). A Duck94 model simulation using the optimum values in Table 1 and a d_{50} = 170 μm for $z < -1.5$ m rather than the z-dependence in Figure 7 did not degrade model skill, consistent with *Gallagher et al.* [1998, Table 1 and Figure 8c] and *Henderson et al.* [2004]. We cannot rule out the possibility that, as shown by *Gallagher et al.* [1998], variable d_{50} is relevant to profile evolution during parts of Duck94 not used here.

[30] The largest differences in observed and predicted evolution of the bed profiles are found for the first storm at Hasaki ($\bar{t}$ = 37.5 days, Figure 8d), when the model underestimates the observed offshore migration and does not reproduce the trough deepening. One of the reasons for these discrepancies may be the nonconserved mass of sand in the cross-shore profile (Figure 2b), which can obviously not be captured using a one-dimensional model. Similar to previous noncoupled model studies [*Hoefel and Elgar*, 2003; *Henderson et al.*, 2004; *Hsu et al.*, 2006], the model underpredicts the onshore bar migration during Duck94,

specifically the increased height of the sandbar crest (Figure 8b). Model skill at the end of this onshore event amounts to 0.73 (Figure 5d), about the same as that based on the noncoupled acceleration-based energetics model of *Hoefel and Elgar* [2003] and the wave-resolving eddy-diffusive model of *Henderson et al.* [2004] [see *Henderson et al.*, 2004, Table 1]. Finally, the model poorly predicts the evolution of the inner bar at Egmond; neither its offshore migration nor the deepening of the inner trough is predicted well (Figure 8l). The difference in inner/outer bar performance is also obvious from the model skill computed separately for the outer ($-600 \leq x \leq -364$ m) and inner ($-362 \leq x \leq -32$ m) bar region (Figure 6d). While at the end of the simulation the outer-bar skill amounts to 0.82, the inner-bar skill is negative (-0.25), implying that the model-produced inner-bar evolution was worse than the no-change model. The onshore reduction in model skill at Egmond was also found by *Van Rijn et al.* [2003] and is consistent with the observed change from alongshore uniform to nonuniform morphology toward shore.

[31] As exemplified for the Duck94 experiment in Figure 9a, the model predicts offshore bar migration during intense wave breaking ($\bar{t}$ = 275–276 days; predicted [*Battjes and Janssen*, 1978] fraction of breaking waves $Q_b \approx 0.3 - 0.7$), while onshore bar migration is produced under energetic, weakly to nonbreaking conditions (e.g., $\bar{t}$ = 270–273 days; $Q_b \approx 0 - 0.3$). Furthermore, the Duck94 bar remains stationary during conditions with alternating breaking and nonbreaking waves during low tide and high tide, respectively ($\bar{t} \approx 269$ days), as well as during small waves ($\bar{t}$ = 273–275 days). A similar dependence of the
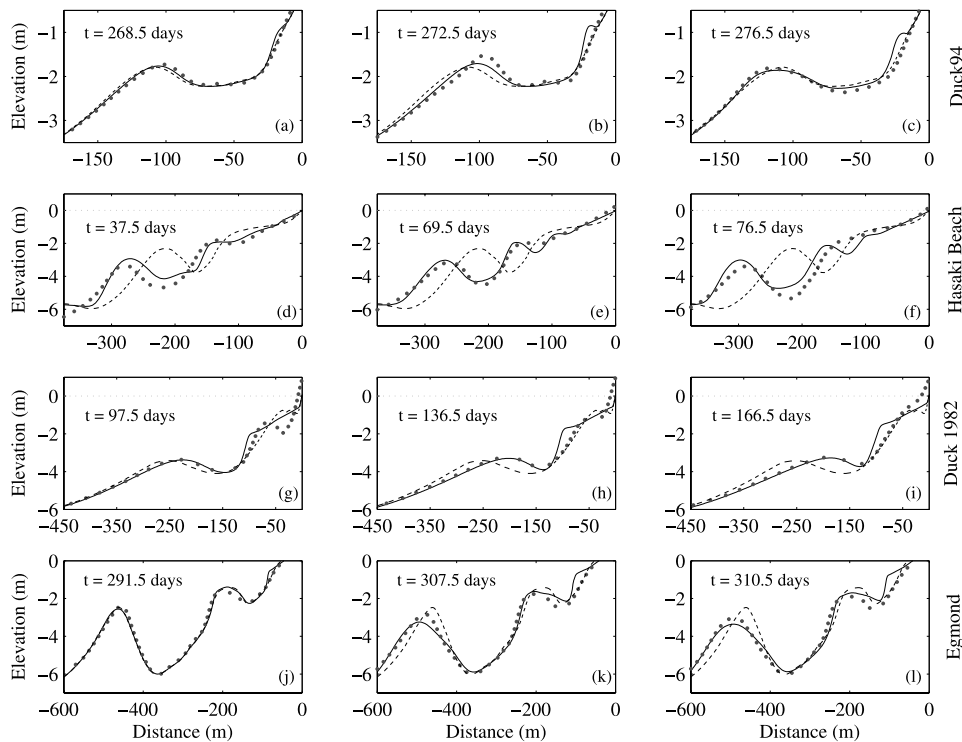

Figure 8. Measured (dots) and modeled (solid line) bed elevation at (a)–(c) Duck94, (d)–(f) Hasaki, (g)–(i) Duck 1982, and (j)–(l) Egmond versus cross-shore distance. The initial profile is shown with the dashed line.
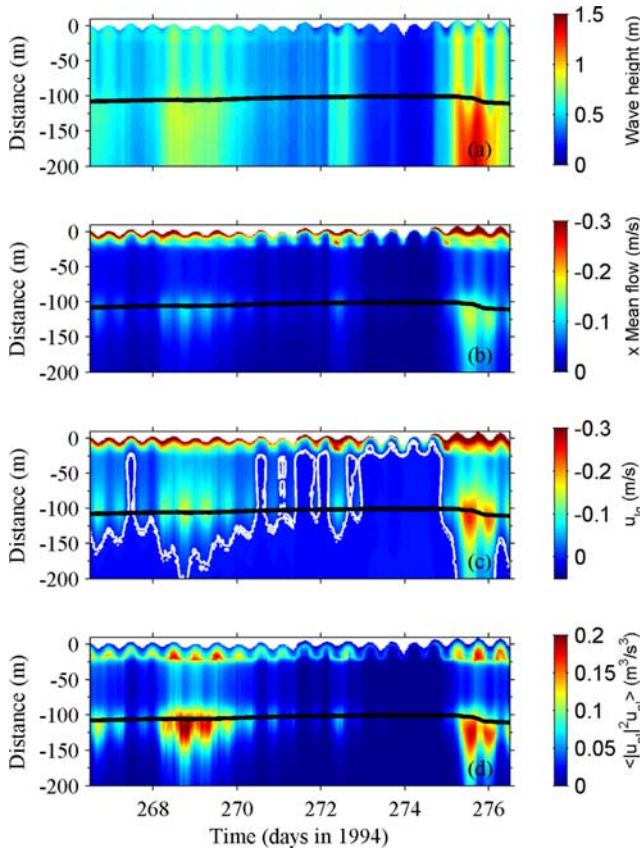
Figure 9. Time-space diagrams of predicted (a) root mean square wave height H_{rms}, (b) depth-averaged cross-shore mean current $\overline{u}$, (c) cross-shore mean current at the lowest vertical grid point $\overline{u}_{lgx}$, and (d) third-order short-wave moment $\langle |u_{nl}^2| u_{nl} \rangle$ at Duck based on the optimum parameter settings. The location of the bar crest is shown with the black line. The white line in Figure 9c is the 0 m/s contour.

direction of bar migration on (breaking) wave conditions is also obvious at the other sites (Figures 2g, 3g, and 6e). Again using the Duck94 model results as an example, peak depth-averaged mean cross-shore currents of about −0.2 m/s occur during low tide when waves break at or just seaward of the bar crest (Figure 9b). Values of $\overline{u}$ at the outer bar at Egmond reach values up to −0.35 m/s during the most intense wave breaking at $\overline{t} = 297.5$ days. The near-bed cross-shore flow ($\overline{u}_{lgx}$) across the bar is generally negative and follows the same temporal evolution as $\overline{u}$ (Figure 9c, compare to Figure 9b). Under small waves only $\overline{u}_{lgx}$ becomes onshore directed near the bar crest (Figure 9c), with maximum values less than 0.01−0.02 m/s.

[32] In standard energetics models [e.g., *Roelvink and Stive*, 1989; *Gallagher et al.*, 1998], bedload depends on $\langle |u_b|^2 u_b \rangle$, with $\langle |u_{nl}|^2 u_{nl} \rangle$ and $3 \langle |u_{nl}|^2 u_{bw} \rangle$ proportional to the transport by skewed waves and bound infragravity waves, respectively. Although these terms are not used in the present sediment transport computations, they may serve to assess the relevance of skewed waves and bound infra-gravity waves to q_{bed}. (Substituting equation (13) into q_{bed} (12) results in a transport dependence on the 3.6 power of velocity, between the third and fourth power dependencies

in the bedload and suspended load terms in energetics models.) The third-order moment $\langle |u_{nl}|^2 u_{nl} \rangle$ is predicted to peak just seaward of the bar during both energetic, non-breaking conditions and breaking waves, with typically larger values at low tide than at high tide (Figure 9d). The predicted magnitude ($0-0.2$ m^3/s^3) and temporal variability of $\langle |u_{nl}|^2 u_{nl} \rangle$ are consistent with observations at Duck based on free-stream (i.e., above the wave boundary layer) orbital velocities (compare present Figure 9d to Figure 5a by *Hsu et al.* [2006]). The predicted magnitude of $3 \langle |u_{nl}|^2 u_{bw} \rangle$ is largest near the bar crest during energetic, weakly to non-breaking conditions. At Duck, $3 \langle |u_{nl}|^2 u_{bw} \rangle$ is 0.5% of $\langle |u_{nl}|^2 u_{nl} \rangle$ at most, increasing to $15-20\%$ at Hasaki (because of nonzero c_r; see Table 1).

[33] The largest net transport magnitudes (and gradients therein) are predicted at the location of wave breaking (Figure 10a, compare to Figure 9a). Superimposed is a tidal fluctuation, with larger magnitudes during low tide than during high tide. During strong wave breaking, the net transport across the bar is offshore directed (Figure 10a), primarily because of the suspended load (Figure 10b), although offshore directed bedload peaking just seaward of the bar crest can be substantial as well (Figure 10c) at low tide. Typically, the model predicts onshore, skewness-induced q_{bed} seaward of the breaker zone, see, for example, Figure 10c at $\overline{t} \approx 276$ days and $x = -200$ to -150 m. The offshore-directed transport across the bar, peaking at the crest, and the onshore-directed transport further offshore causes the bar to move offshore and to develop a somewhat steeper seaward flank. Because of the coupled nature of our model, this seaward bar shift results in a seaward shift of the breaker zone (Figure 9a), location of maximum undertow
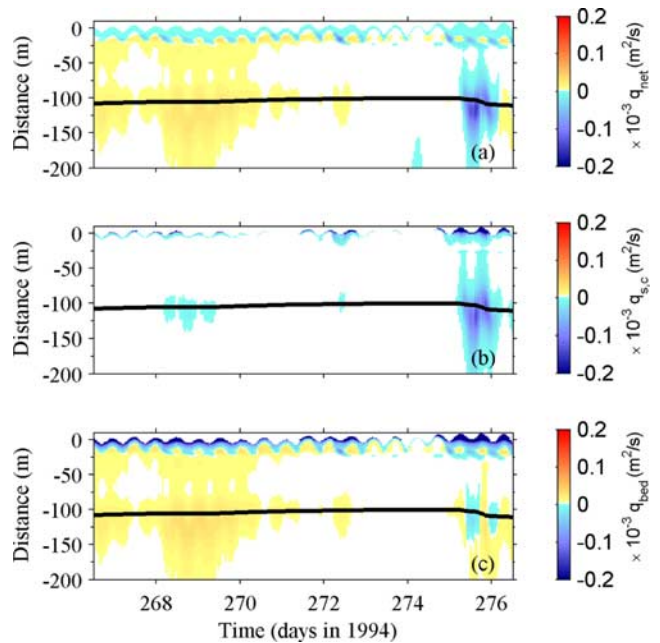

Figure 10. Time-space diagrams of predicted (a) net transport rate q_{net}, (b) current-related suspended transport rate $q_{s,c}$, and (c) bedload transport rate q_{bed} during the Duck94 experiment based on the optimum parameter settings. The location of the bar crest is shown with the black line.

(Figure 9b), and offshore directed transport (Figure 10a), until wave breaking on the bar ceases at the end of the storm. The feedback driving the bar offshore when large waves in storms break on the bar is thus identical to the feedback found in noncoupled model experiments [e.g., *Thornton et al.*, 1996; *Gallagher et al.*, 1998].

[34] During energetic, weakly to nonbreaking conditions the model predicts onshore-directed q_{net} that is maximum at (high tide) or just offshore of (low tide) the bar crest (Figure 10a, $\bar{t}$ = 270–273 days). The onshore direction is induced primarily by the skewness of the near-bed orbital flow; the contribution of infragravity waves to the transport is negligible (Duck and Egmond) to small (Hasaki), and $\bar{u}_{lgx}$ is weak and offshore directed, suggesting that near-bed streaming is not very relevant to the simulated onshore bar migration. The feedback between the bed and the onshore sediment transport peaking at the bar results in onshore bar migration until the waves become small and bar migration ceases. When breaking and nonbreaking conditions alternate at low and high tide (such as during the peak of the swell event during Duck94, $\bar{t} \approx 269$ days, Figure 9a and during several storms during Duck 1982, for instance, $\bar{t} \approx 58$ and 118 days, Figure 3g) the bar remains stationary over the tidal cycle because offshore migration during low tide is largely undone by onshore migration at high tide.

[35] When waves are small, net transport rates are minimal and the bar remains stationary (e.g., Figure 10a, $\bar{t}$ = 273–274 days). When viewed in more detail, the model predicts weak offshore q_{bed} (and q_{net}) seaward of the bar. This gravity-induced downslope transport is most pronounced in the Hasaki data set because of the rather low optimum $\tan\phi$ of ≈ 0.15 (Table 1). The feedback between the gravity-induced transport and the seabed invokes the flattening of the seaward side of the bar as it arrives in deeper water.

5. Discussion

5.1. Wave-Averaged Versus Wave-Resolving Approach

[36] In this paper we have developed and tested a one-dimensional wave-averaged bed evolution model. Clearly, wave-resolving models may be more accurate representations of nearshore hydrodynamics and sediment transport. For instance, Boussinesq models have now reached the stage of applicability from intermediate water through the surf zone to the shoreline [*Kirby*, 2003; *Long et al.*, 2004], and may provide more accurate predictions of near-bed short-wave nonlinearity than the presently adopted *Rienecker and Fenton* [1981] stream function theory (that ignores wave asymmetry) with input from a simple, linear wave model. The main advantage of our wave-averaged parameterizations of intrawave processes is that they allow morphological predictions at the timescale of variability in the wave forcing, O(hours-weeks). Note that, typically, $\partial \bar{t}$ is about 0.1 s (1 hr) in a wave-resolving (wave-averaged) approach. Wave-averaged models can thus be applied for complicated cases (that is, onshore and offshore sandbar migration on the timescales of days to weeks, or even longer), while complicated, Boussinesq-based coupled models have sofar only been applied to laboratory [e.g., *Rakha et al.*, 1997] or short (a few days maximum) field cases [e.g., *Long et al.*, 2004]. Our parameterizations are

still physically reasonable, and capture many of the essential aspects of nearshore hydrodynamics and sediment transport, as indicated by the moderate to high skill (0.50–0.88) in hindcasting observed on/offshore sandbar migration.

5.2. Free Parameters

[37] Similar to existing noncoupled [*Gallagher et al.*, 1998; *Henderson et al.*, 2004; *Hoefel and Elgar*, 2003] and wave-resolving [e.g., *Long et al.*, 2004] models, we have to specify values for various free parameters. We limited the calibration to those parameters that we considered to be most uncertain. The breaking-wave parameter γ was, for instance, not a free parameter, because the applied γ parameterization was estimated from the observed cross-shore distribution of H_{rms} of the Duck94 experiment (using the measured seafloor evolution and $\alpha = 1$) and subsequently validated on a number of other data sets, including the present Egmond data [*Ruessink et al.*, 2003]. The roller slope $\beta = 0.1$ was based on laboratory studies of setup, undertow, and alongshore currents [*Nairn et al.*, 1990; *Reniers and Battjes*, 1997].

[38] In contrast, we had little guidance to *a priori* determine realistic values or parameterizations for α_w, c_r, $\tan\phi$, and k_c. The available flow measurements at Duck94 [e.g., *Feddersen et al.*, 1998] and Egmond [*Ruessink et al.*, 2001] are insufficient to test the undertow model because of the uncertainty in the sensor elevations above the seafloor, the sensitivity of the undertow magnitude to these elevations, and the generally poor resolution of the sensors in the vertical and, at Egmond, in the cross-shore. Calibrations of the undertow model using vertical velocity profiles obtained during another Duck campaign [*Reniers et al.*, 2004] showed that the depth-averaged cross-shore flow below the wave trough level can be predicted well with equation (5) in case of alongshore uniformity in morphology and that the vertical structure is simulated well for $\alpha_w \approx 0.1$. With the present optimum α_w, the predicted range of the depth-averaged viscosity ($0 < \bar{\nu}_t < 0.05$ m^2/s at Hasaki and Duck and $0 < \bar{\nu}_t < 0.17$ m^2/s at Egmond) is in line with estimates inferred from measured mean cross-shore currents across barred beaches [e.g. *Haines and Sallenger*, 1994; *Garcez Faria et al.*, 2000]. Thus, although α_w was estimated here by a model calibration on bed evolution, the obtained values suggest that the predicted vertical structure of the cross-shore mean flow was realistic. Also, the predicted negligible to minor contribution of bound infragravity waves to the bedload ($c_r \approx 0$) is consistent with observations of sediment fluxes [e.g., *Conley and Beach*, 2003; *Ruessink et al.*, 1998] and third-order velocity moments [e.g., *Thornton et al.*, 1996; *Russell and Huntley*, 1999].

5.3. Intersite Parameter Differences

[39] The intersite differences in optimum parameter values (Table 1) are likely due to a mixture of model structure error, including poorly described or missing processes, model insensitivity to parameters, parameter interdependence, and errors in the wave and water level forcing.

[40] *Hsu et al.* [2006] demonstrated that parameters can adjust for missing processes. We have, for instance, not considered the relevance of free infragravity waves, the mass failure of the upper layer of the sand bed ("plug
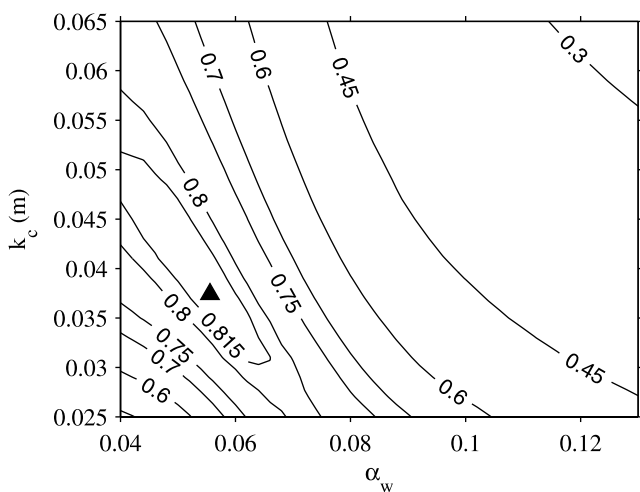
Figure 11. Skill R surface of α_w versus k_c (based on $c_r = 0.09$ and $\tan\phi = 0.14$) for the Hasaki beach data set at $\bar{t} = 76.5$ days. The triangle represents the best fit value found by the SCE-UA algorithm. The skill surface was constructed by performing 2750 computations sampled from the indicated $k_c - \alpha_w$ subspace using a Latin hypercube sampling strategy.

flow") [*Foster et al.*, 2006], and the stirring of sediment by the surface breaking-induced turbulence penetrating toward the bottom [e.g., *Roelvink and Stive*, 1989] to onshore and offshore bar migration. When such model-structure errors have different relevance between the sites, the search algorithm may have compensated for this deficiency but this results in different intersite values of the parameters optimized.

[41] Results of sensitivity tests (not shown) indicated that the model is largely insensitive to $\tan\phi$ for $\tan\phi > \approx 0.25$. The $\tan\phi$ values for both Duck simulations therefore may be nonunique, enforced primarily by the different random seed in the set-up of SCE-UA. The nonconcentric contours in the example error surface given in Figure 11 indicate an $\alpha_w - k_c$ interdependence, implying that at each site a relatively wide range of $\alpha_w - k_c$ combinations yields comparable model skill. Apparently, a $q_{s,c}$ reduction resulting from an increase in α_w can be undone by a simultaneous decrease in k_c, resulting in about the same $q_{s,c}$ and model performance. Parameter interdependence frustrates model calibration owing to premature convergence at nonunique parameter values (that is, somewhere on the $\alpha_w - k_c$ ridge depending on the random seed in SCE-UA rather than the true optimum), because only little progress can be made along the ridge toward its highest point.

[42] The effect of errors in the wave forcing on optimum parameter values is demonstrated in Figure 12. The Duck 1982 model calibrations were repeated with four different time-independent offshore wave angles ($10°–40°$, with a $10°$ increment) with k_c as the only free parameter, leaving the remaining three parameters at their optimum $0°$ value. As shown in Figure 12a, model skill is independent of the offshore wave angle, but optimum k_c reduces with θ (Figure 12b). An increase in θ reduces the wave height at the bar because of refractional effects. For the same bed profile and offshore wave height, period, and water level,

this wave height reduction at the bar reduces local $q_{s,c}$ more than it reduces q_{bed}. The calibration algorithm responds by increasing $q_{s,c}$ by reducing k_c. This k_c reduction ensures the same q_{net}, bed evolution, and model skill as found for $\theta = 0°$. Thus parameters can adjust for model errors invoked by errors in the boundary forcing. The different sources of boundary errors (e.g., some sites had nondirectional wave sensors or lacked measured water levels) may have contributed to the intersite variability in parameter values.

[43] The foregoing discussion has shown that parameters may, at least partly, compensate for model structure errors and errors in the boundary forcing. This implies that model-parameters should not be confused with their physical analogues, a situation that is not helped by the fact that both often have the same name. Although we cannot rule out the possibility that unknown intersite differences in bed form characteristics owing to differences in grain size and wave conditions may have contributed to the k_c variability, we doubt whether a realistic bedform and roughness predictor would actually improve the skill of the present model. At present, α_w, c_r, $\tan\phi$, and k_c are best interpreted as free model parameters that, when chosen appropriately, yield reasonably accurate predictions of both erosion and accretion.

[44] The various sources of intersite parameter variability have different importance between the sites. Consequently, we expect that a single optimum parameter set that results in accurate on/offshore bar migration at all 4 sites will not exist. To examine this further, we performed a calibration run in which we optimized model skill for all four sites simultaneously by tuning k_c and using "site-averaged" $c_r = 0$ (Table 1), $\tan\phi = 0.25$ (Table 1), and $\alpha_w = 0.1$ [*Reniers et*
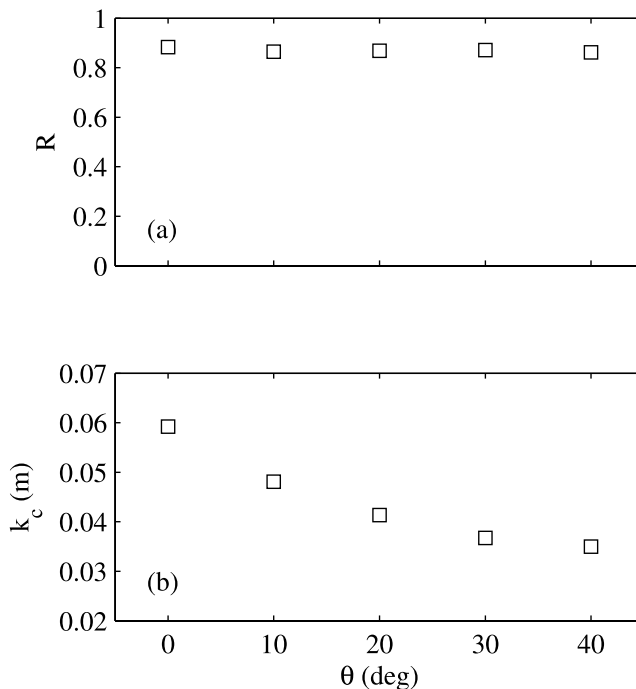

Figure 12. (a) Skill R at $\bar{t} = 166.5$ days and (b) optimum current-related roughness k_c versus the time-independent offshore wave angle in the Duck 1982 simulations.

al., 2004]. The optimum k_c (≈ 0.04 m) results in a prediction skill decay at all sites, in particular at Egmond ($R = -3.5$) and Hasaki ($R = 0.32$). The model now overpredicts the offshore migration of the outer Egmond sandbar with some 80 m, while, in contrast, the model underpredicts the offshore migration at Hasaki with about 40 m. In contrast, the prediction skill for the onshore event at Duck 1982 ($R = 0.83$) reduces only slightly relative to the skill based on the Duck 1982 optimum values. The changes in k_c and α_w relative to the site-dependent optimum values primarily affect the current-related suspended flux; when this flux dominates the net flux (which is the case in the Egmond and Hasaki data sets), the use of site-averaged values will thus reduce skill most. On the whole, these results confirm our expectation that we cannot predict bathymetric change in the field accurately with a "default" set of parameters; bathymetric data of the investigation site or of a nearby coast, preferably encompassing both an onshore and offshore event, are required to tune the model's parameters to accommodate for site-specific errors.

5.4. Onshore Bar Migration

[45] Despite the intersite parameter differences, the relative importance of the various hydrodynamical processes to the net sediment transport was robust. Similar to earlier observations and predictions based on other sediment transport equations, simulated offshore bar migration took place during energetic, breaking conditions and was largely due to the feedback among morphology, waves, undertow, and suspended sediment transport. Predicted shoreward bar migration was simulated under energetic, weakly to nonbreaking conditions and was driven by a similar feedback involving the onshore bedload transport induced primarily by skewed near-bed orbital wave motion. The relevance of near-bed skewness to onshore bar migration differs from the near-zero bar-migration results from energetics-based models [*Gallagher et al.*, 1998], in which the inclusion of an empirical fluid-acceleration parameter is required to simulate onshore bar migration realistically [*Hoefel and Elgar*, 2003]. Wave boundary layer simulations by *Henderson et al.* [2004] show that when mean currents are weak and the free-stream orbital motion is asymmetric, the wave-induced sediment flux is correlated strongly with the cube of the near-bed (that is, within the wave boundary layer) flow ($\langle |u_{nl}|^2 u_{nl} \rangle$ in Section 4) because of a phase shift that converts free-stream asymmetry to near-bed skewness. Our model simulations show that, consistent with findings by *Hsu et al.* [2006], realistic onshore bar migration can be obtained using a sediment transport model based on near-bed skewness without a description of free-stream asymmetry and the phase shift in the wave boundary layer. *Hsu et al.*'s [2006] quasi-steady model (essentially, the wave-resolving version of our equations (12) and (13) driven with observed free-stream velocities) has similar skill in predicting the onshore bar event at Duck94 as a linear boundary layer model capturing the boundary layer phase change, suggesting that velocity skewness is sufficient to predict onshore bar migration. Their nonlinear wave boundary layer model, which includes boundary layer streaming, resulted in improved skill specifically on the steep foreshore (T. J. Hsu, personal communication, 2005), suggesting that, consistent with our results, streaming is not crucial for onshore bar

migration. Detailed observations of concentration and velocity profiles under a wide range of conditions are required to properly validate the temporal and spatial variability of q_{bed} and $q_{s,c}$ as predicted by the present formulations.

6. Conclusions

[46] We have presented and evaluated a coupled, wave-averaged, cross-shore waves-currents-bathymetric evolution model using data gathered at the barred beaches of Duck (N. C., USA), Hasaki (Kashima Coast, Japan), and Egmond (Netherlands). Reliable simulations of observed onshore and offshore bar migration, and associated changes in the cross-shore bar shape, are obtained by tuning four free parameters in the undertow and sediment transport models. Model skill ranges from 0.50 at Egmond, where the model does not reproduce observed inner-bar migration well, to 0.88 for the 3.5-month onshore bar migration event at Duck. In contrast to the coupled model results by *Plant et al.* [2004], the present model does not require temporal changes in the free model parameters to make significant predictions of combined on/offshore sandbar migration. Localized (in time and space) reductions in model skill coincide with alongshore variations in the observed morphology. The intersite differences in the optimum parameter values are, at least partly, related to insensitivity to parameter variations, parameter interdependence, and errors in the offshore wave and water level forcing.

[47] Consistent with earlier observations, the model simulates offshore bar migration when large waves during storms break on the bar. The breaking causes strong offshore currents (undertow) that peak at or just seaward of the sandbar crest, and the offshore migration is driven by the associated gradients in the suspended sediment transport. Onshore bar migration is predicted for energetic, weakly to nonbreaking conditions and is due primarily to the feedback among near-bed wave skewness, bedload transport, and the sandbar, with negligible effects of bound infragravity waves and near-bed streaming. The simulations suggest that realistic onshore bar migration can be obtained using a nonlinear wave theory that neglects free-stream asymmetry and the phase shift that converts free-stream asymmetry to near-bed skewness in the wave boundary layer. Under small waves, the sandbar is predicted to remain stationary; downslope gravity-induced transport reduces the slope of the seaward flank of the sandbar. When breaking and nonbreaking waves alternate during low tide and high tide, the net sandbar migration over the tidal cycle is almost nil. Because the calibration procedure focuses on net sediment transport rates only and parameters may compensate for missing or incompletely described processes, it is imperative to collect concentration and velocity profiles under a wide range of natural conditions to test the relevance of the suggested hydrodynamical processes to offshore and onshore sandbar migration.

References

Battjes, J. A., and J. P. F. M. Janssen (1978), Energy loss and set-up due to breaking of random waves, in *Proceedings of Sixteenth Coastal Engineering Conference*, pp. 570–587, Am. Soc. of Civ. Eng., New York.

Battjes, J. A., and M. J. F. Stive (1985), Calibration and verification of a dissipation model for random breaking waves, *J. Geophys. Res.*, *90*, 9159–9167.

Bosboom, J., S. G. J. Aarninkhof, A. J. H. M. Reniers, J. A. Roelvink, and D. J. R. Walstra (1997), Unibest-TC 2.0. overview of model formulations, *Rep. H2305.42*, WL|Delft Hydraulics, Delft, Netherlands.

Brøker Hedegaard, I., R. Deigaard, and J. Fredsøe (1991), On/offshore sediment transport and morphological modelling of coastal profiles, in *Proceedings of Coastal Sediments'91*, pp. 643–657, Am. Soc. of Civ. Eng., New York.

Conley, D. C., and R. A. Beach (2003), Cross-shore sediment transport partitioning in the nearshore during a storm event, *J. Geophys. Res.*, *108*(C3), 3065, doi:10.1029/2001JC001230.

Dally, W. R. (1987), Longshore bar formation: Surf beat or undertow, in *Proceedings of Coastal Sediments'87*, pp. 71–86, Am. Soc. of Civ. Eng., New York.

Dally, W. R., and R. G. Dean (1984), Suspended sediment transport and beach profile evolution, *J. Waterw. Port Coastal Ocean Eng.*, *110*, 15–33.

Duan, Q., V. K. Gupta, and S. Sorooshian (1993), A shuffled complex evolution approach for effective and efficient optimization, *J. Optim. Theory Appl.*, *76*, 501–521.

Feddersen, F., R. T. Guza, S. Elgar, and T. H. C. Herbers (1998), Along-shore momentum balances in the nearshore, *J. Geophys. Res.*, *103*, 15,667–15,676.

Foster, D. L., A. J. Bowen, R. A. Holman, and P. Natoo (2006), Field evidence of pressure gradient induced incipient motion, *J. Geophys. Res.*, *111*, C05004, doi:10.1029/2004JC002863.

Fredsøe, J., and R. Deigaard (1992), *Mechanics of Coastal Sediment Transport*, World Sci., Singapore.

Gallagher, E. L., S. Elgar, and R. T. Guza (1998), Observations of sand bar evolution on a natural beach, *J. Geophys. Res.*, *103*, 3203–3215.

Garcez Faria, A. F., E. B. Thornton, T. C. Lippmann, and T. P. Stanton (2000), Undertow over a barred beach, *J. Geophys. Res.*, *105*, 16,999–17,010.

Haines, J. W., and A. H. Sallenger (1994), Vertical structure of mean cross-shore currents across a barred surf zone, *J. Geophys. Res.*, *99*, 14,223–14,242.

Henderson, S. M., J. S. Allen, and P. A. Newberger (2004), Nearshore sandbar migration predicted by an eddy-diffusive boundary layer model, *J. Geophys. Res.*, *109*, C06024, doi:10.1029/2003JC002137.

Hoefel, F., and S. Elgar (2003), Wave-induced sediment transport and sandbar migration, *Science*, *299*, 1885–1887.

Hsu, T. J., S. Elgar, and R. T. Guza (2006), Wave-induced sediment transport and onshore sandbar migration, *Coastal Eng.*, *53*, 817–824.

Katoh, K., and S. Yanagishima (1995), Changes of sand grain distribution in the surf zone, in *Proceedings of Coastal Dynamics'95*, pp. 639–650, Am. Soc. of Civ. Eng., New York.

Kirby, J. T. (2003), Boussinesq models and applications to nearshore wave propagation, surfzone processes and wave-induced currents, in *Advances in Coastal Modeling*, edited by V. C. Lakhan, pp. 1–41, Elsevier, Amsterdam.

Kuriyama, Y. (2002), Medium-term bar behavior and associated sediment transport at Hasaki, Japan, *J. Geophys. Res.*, *107*(C9), 3132, doi:10.1029/2001JC000899.

Kuriyama, Y., Y. Ito, and S. Yanagishima (2005), Field investigation on cross-shore distribution of predominant longshore current velocity (in Japanese), *Doboku Gakkai Ronbunshu*, *803/II-73*, 145–153.

Long, W., T. J. Hsu, and J. T. Kirby (2004), Modeling cross-shore sediment transport processes with a time domain Boussinesq model, in *Proceedings of the 29th International Conference on Coastal Engineering*, pp. 1874–1886, Am. Soc. of Civ. Eng., New York.

Nairn, R. B., J. A. Roelvink, and H. N. Southgate (1990), Transition zone width and implications for modelling surfzone hydrodynamics, in *Proceedings of the 22nd International Conference on Coastal Engineering*, pp. 68–82, Am. Soc. of Civ. Eng., New York.

Plant, N. G., K. T. Holland, J. A. Puleo, and E. L. Gallagher (2004), Prediction skill of nearshore profile evolution models, *J. Geophys. Res.*, *109*, C01006, doi:10.1029/2003JC001995.

Plant, N. G., K. T. Holland, and R. A. Holman (2006), A dynamical attractor governs beach response to storms, *Geophys. Res. Lett.*, *33*, L17607, doi:10.1029/2006GL027105.

Rakha, K. A., R. Deigaard, and I. Brøker (1997), A phase-resolving cross-shore sediment transport model for beach profile evolution, *Coastal Eng.*, *31*, 231–261.

Ranasinghe, R., G. Symonds, K. Black, and R. Holman (2004), Morpho-dynamics of intermediate beaches: A video imaging and numerical modelling study, *Coastal Eng.*, *51*, 629–655.

Reniers, A. J. H. M., and J. A. Battjes (1997), A laboratory study of long-shore currents over barred and non-barred beaches, *Coastal Eng.*, *30*, 1–22.

Reniers, A. J. H. M., E. B. Thornton, T. P. Stanton, and J. A. Roelvink (2004), Vertical flow structure during Sandy Duck: Observations and modeling, *Coastal Eng.*, *51*, 237–260, doi:10.1016/j.coastaleng.2004.02.001.

Ribberink, J. S. (1998), Bed-load transport for steady flows and unsteady oscillatory flows, *Coastal Eng.*, *34*, 59–82.

Rienecker, M. M., and J. D. Fenton (1981), A Fourier approximation for steady water waves, *J. Fluid Mech.*, *104*, 119–137.

Roelvink, J. A., and I. Brøker (1993), Cross-shore profile models, *Coastal Eng.*, *21*, 163–191.

Roelvink, J. A., and M. J. F. Stive (1989), Bar-generating cross-shore flow mechanisms on a beach, *J. Geophys. Res.*, *94*, 4785–4800.

Roelvink, J. A., T. J. G. P. Meijer, K. Houwman, R. Bakker, and R. Spanhoff (1995), Field validation and application of a coastal profile model, in *Proceedings of Coastal Dynamics'95*, pp. 818–828, Am. Soc. of Civ. Eng., New York.

Ruessink, B. G. (2005), Calibration of nearshore process models: Application of a hybrid genetic algorithm, *J. Hydroinformatics*, *7*, 135–149.

Ruessink, B. G., K. T. Houwman, and P. Hoekstra (1998), The systematic contribution of transporting mechanisms to the cross-shore sediment transport in water depths of 3 to 9 m, *Mar. Geol.*, *152*, 295–324.

Ruessink, B. G., I. M. J. Van Enckevort, K. S. Kingston, and M. A. Davidson (2000), Analysis of observed two- and three-dimensional nearshore bar behaviour, *Mar. Geol.*, *169*, 161–183.

Ruessink, B. G., J. R. Miles, F. Feddersen, R. T. Guza, and S. Elgar (2001), Modeling the alongshore current on barred beaches, *J. Geophys. Res.*, *106*, 22,451–22,463.

Ruessink, B. G., D. J. R. Walstra, and H. N. Southgate (2003), Calibration and verification of a parametric wave model on barred beaches, *Coastal Eng.*, *48*, 139–149.

Russell, P. E., and D. A. Huntley (1999), A cross-shore transport shape function for high energy beaches, *J. Coastal Res.*, *15*, 198–205.

Sand, S. E. (1982), Long wave problems in laboratory models, *J. Waterw. Port Coastal Ocean Div. Am. Soc. Civ. Eng.*, *108*, 492–503.

Sato, S., and N. Mitsunobu (1991), A numerical model of beach profile change due to random waves, in *Proceedings of Coastal Sediments'91*, pp. 674–687, Am. Soc. Civ. Eng., New York.

Soulsby, R. L. (1997), *Dynamics of Marine Sands*, Thomas Telford, London.

Stauble, D. K., and M. A. Cialone (1996), Sediment dynamics and profile interactions: Duck94, in *Proceedings of the 25th International Conference on Coastal Engineering*, pp. 3921–3934, Am. Soc. Civ. Eng., New York.

Stive, M. J. F. (1986), A model for cross-shore sediment transport, in *Proceedings of the 20th International Conference on Coastal Engineering*, pp. 1550–1564, Am. Soc. Civ. Eng., New York.

Stive, M. J. F., and J. A. Battjes (1984), A model for offshore sediment transport, in *Proceedings of the 19th International Conference on Coastal Engineering*, pp. 1420–1436, Am. Soc. Civ. Eng., New York.

Stive, M. J. F., and H. J. De Vriend (1994), Shear stress and mean flow in shoaling and breaking waves, in *Proceedings of the 24th International Conference on Coastal Engineering*, pp. 594–608, Am. Soc. Civ. Eng., New York.

Takewaka, S. (2005), Measurements of shoreline positions and intertidal foreshore slopes with X-band marine radar system, *Coastal Eng. J.*, *47*, 91–107.

Thornton, E. B., R. T. Humiston, and W. Birkemeier (1996), Bar/trough generation on a natural beach, *J. Geophys. Res.*, *101*, 12,097–12,110.

Trowbridge, J., and D. Young (1989), Sand transport by unbroken water waves under sheet flow conditions, *J. Geophys. Res.*, *94*, 10,971–10,991.

Van Rijn, L. C. (1993), *Principles of Sediment Transport in Rivers, Estuaries and Coastal Seas*, Aqua, Amsterdam.

Van Rijn, L. C. (1995), Yearly averaged sand transport at the 20 m and 8 m NAP depth contours of the JARKUS profiles 14, 40, 76 and 103, *Rep. H1887*, Delft Hydraulics, Delft, Netherlands.

Van Rijn, L. C., B. G. Ruessink, and J. P. M. Mulder (2002), *Coast3D-Egmond: The Behaviour of a Straight Sandy Coast on the Time Scale of Storms and Seasons*, Aqua, Amsterdam.

Van Rijn, L. C., D. J. R. Walstra, B. Grasmeijer, J. Sutherland, S. Pan, and J. P. Sierra (2003), The predictability of cross-shore bed evolution of sandy beaches at the time scale of storms and seasons using process-based profile models, *Coastal Eng.*, *47*, 295–327.

————————————

Y. Kuriyama, Littoral Drift Division, Port and Airport Research Institute, Yokosuka 239-0826, Japan. (kuriyama@pari.go.jp)

A. J. H. M. Reniers, Division of Applied Marine Physics, Rosenstiel School of Marine and Atmospheric Science, University of Miami, 4600 Rickenbacker Causeway, Miami, FL 33149–1098, USA. (areniers@rsmas.miami.edu)

J. A. Roelvink, UNESCO-IHE Institute for Water Education, P.O. Box 3015, NL-2601 DA Delft, Netherlands. (d.roelvink@unesco-ihe.org)

B. G. Ruessink, Department of Physical Geography, Faculty of Geosciences, Institute for Marine and Atmospheric Research Utrecht, Utrecht University, P.O. Box 80.115, NL-3508 TC Utrecht, Netherlands. (g.ruessink@geo.uu.nl)

D. J. R. Walstra, Marine and Coastal Management, WL|Delft Hydraulics, P.O. Box 177, NL-2600 MH Delft, Netherlands. (dirkjan.walstra@wldelft.nl)